Title

De novo design of a transmembrane Zn2+-transporting four-helix bundle

Authors

Joh, Nathan H
Wang, Tuo
Bhate, Manasi P
et al.

Peer reviewed

De novo design of a transmembrane Zn^{2+}-transporting four-helix bundle

Nathan H. Joh[1], **Tuo Wang**[2], **Manasi P. Bhate**[1], **Rudresh Acharya**[3], **Yibing Wu**[1], **Michael Grabe**[1,*], **Mei Hong**[2,*], **Gevorg Grigoryan**[4,*], and **William F. DeGrado**[1,*]

[1]Department of Pharmaceutical Chemistry, Cardiovascular Research Institute, University of California, San Francisco, San Francisco, CA 94158, USA

[2]Department of Chemistry, Massachusetts Institute of Technology, Cambridge, MA 02139, USA

[3]School of Biological Sciences, National Institute of Science Education and Research, Bhubaneswar, Odisha, India

[4]Department of Computer Science and Department of Biological Sciences, Dartmouth College, Hanover, NH 03755, USA

Abstract

The design of functional membrane proteins from first principles represents a grand challenge in chemistry and structural biology. Here, we report the design of a membrane-spanning, four-helical bundle that transports first-row transition metal ions Zn^{2+} and Co^{2+}, but not Ca^{2+}, across membranes. The conduction path was designed to contain two di-metal binding sites that bind with negative cooperativity. X-ray crystallography and solid-state and solution nuclear magnetic resonance indicate that the overall helical bundle is formed from two tightly interacting pairs of helices, which form individual domains that interact weakly along a more dynamic interface. Vesicle flux experiments show that as Zn^{2+} ions diffuse down their concentration gradients, protons are antiported. These experiments illustrate the feasibility of designing membrane proteins with predefined structural and dynamic properties.

The de novo design of proteins is an important endeavor that critically tests our understanding of the principles underlying protein folding and function, while also laying the foundation for the design of proteins and molecular assemblies with desired properties. Much progress has been recently demonstrated in the design of water-soluble proteins with a

SUPPLEMENTARY MATERIALS

www.sciencemag.org/content/346/6216/1520/suppl/DC1

Materials and Methods

Figs. S1 to S6

Tables S1 to S5

References (43–67)

variety of folds (1), and numerous natural proteins have been redesigned to bind metal ions (2) or small molecules (3) or to catalyze mechanistically simple reactions (4–7). However, the design of membrane proteins remains in its infancy (8, 9). To date, the most complex designed membrane proteins contain porphyrins that catalyze transmembrane electron transfer (8), but no designed membrane protein has been experimentally shown to adopt the desired fold at atomic resolution.

Here, we focus on the design of a Zn^{2+} transporter, a goal that presents several challenges. First is to design a membrane protein with a predefined structure and, second, to determine its structure and dynamics at high resolution. Next, the design must precisely position polar ionizable Zn^{2+} ligands, which are ordinarily excluded from a membrane environment. Furthermore, proton-Zn^{2+} antiport requires thermodynamic coupling to link proton binding to changes in metal ion affinity. Finally, we aimed to anticipate and orchestrate dynamics to facilitate ion transport.

Here, we describe a computational strategy for the design of a Zn^{2+} transporter, dubbed Rocker, to characterize its structure, and demonstrate that it transports Zn^{2+} with concomitant reverse transport of protons. This work demonstrates the feasibility of membrane protein design and suggests that the advances recently reported in the design of water-soluble proteins can now be extended to membrane-spanning structures.

Natural transporters are hypothesized to rock between two or more states in a mechanism known as alternating access (10–12). For example, the multidrug transporter EmrE is a homodimer that is not stable in a single symmetric homodimeric conformation (13). Instead, it rocks between two degenerate asymmetric structures that alternately expose a substrate-binding site to the cytoplasmic and periplasmic sides of the membrane. Many transporters also harness the energy released in the movement of one ion down its concentration gradient to drive the accumulation of a second ion or small molecule. In proton-dependent transporters, protons often compete directly with substrates for binding to ionizable side chains. We sought to design a minimal protein that uses a similar mechanism. Four-helix bundles are capable of transporting protons (14–16) and binding metal ions, so we focused on this fold. Moreover, we previously observed that the Glu side chains in a 4Glu-2His di-Zn^{2+}–binding protein were largely protonated, even at neutral pH, in the absence of Zn^{2+}, because of the energetic cost of burying negatively charged side chains within the interior of a protein (17). Binding of Zn^{2+} displaces these protons, providing a means to achieve the desired thermodynamic coupling. Moreover, di-metal sites often have bridging water or hydroxide ligands, which could provide kinetically accessible sites for passing protons to the protein ligands as they diffuse through the channel.

We focused on design of a four-helix bundle with the helices inclined by a 10° to 20° angle (Fig. 1, A to D, and fig. S1); if the helices are straight, they diverge from a point of closest approach to yield a truncated conical shape. However, if they gently curve (as in a coiled-coil), the bundle has a more cylindrical shape. An appropriately designed antiparallel homo-tetramer might alternate between the two energetically equivalent asymmetric conformations with the wider end at one or the other side of the bundle. The highly symmetric coiled-coil might provide an intermediate state, facilitating movement of ions through the bundle (Fig.

1A). However, the coiled-coil should not be so stable as to kinetically trap the mobile ions. Thus, the process reduces to the design of an energy landscape in which the two degenerate asymmetric states are more stable than the symmetric coiled-coil.

We chose a homotetrameric bundle with two 2His4Glu di-Zn^{2+}–binding sites, each site formed by the coalescence of an EXXH motif near the N terminus of two helices and a Glu near the C terminus of the other two helices (Fig. 1, A and B). The symmetric coiled-coil was designed via a stochastic search in the space of Crick parameters (18, 19) to find a backbone conformation that allowed Zn^{2+} binding in a good geometry (20, 21). Moreover, we assured that the helix-helix interfaces would be "designable"; i.e., their backbone geometries should be well represented in a diverse set of native proteins (see fig. S1, E and F, and supplementary methods) (19). The resulting 25-residue-long antiparallel homotetrameric bundle shares no structural similarities with YiiP, the only natural Zn^{2+} transporter with a high-resolution structure (22). YiiP is a hexamer with a single 1His3Asp Zn^{2+} site.

We next created the off-symmetry version of the bundle by straightening helices beyond the boundaries of one metal-binding site, which caused subtle flaring of the bundle (up to 1.7 Å) and distorted the binding site at the opposite end of the oligomer (Fig. 1A). To stabilize this conformation relative to the symmetric coiled-coil, we used a negative design algorithm (23). This was a difficult task, given the high similarity between the structures. Negative design relies in part on introducing interactions to destabilize the symmetric conformation. If the backbone relaxes even subtly in an unanticipated manner, these interactions may become much less destabilizing. Moreover, conformational entropy may be significant for encoding preference for the asymmetric state. To address these issues, we defined configuration-space volume elements around the symmetric and asymmetric structures, and we used VALOCIDY (24) to estimate the free energy in each for the top ~1000 sequences predicted to be asymmetry-selective by initial negative design (NVT ensemble, IMM1 force field) (25). The final sequence chosen (Fig. 1C) was the one displaying the largest VALOCIDY-estimated free-energy difference between the two states, while having a sufficiently large pore to permit ion conduction. Residues allowed in design were defined, based on membrane depth using the E_Z potential (table S1) (26, 27). We also required a second-shell H-bond to the metal binding His (28) (see supplementary methods for details).

The resulting dimer of dimers has two nonequivalent helix-helix interfaces (Fig. 1D); a "tight interface" has a small interhelical distance (8.9 Å) stabilized by efficient packing of small, Ala residues. The geometry of the tight interface is similar to the "alanine coil," a sequence-structure motif shown to impart thermodynamic stability and structural rigidity in model peptides (29). The "loose interface" has a larger interhelical distance of 12.0 Å packed by large Phe residues. The packing of large apolar residues in membrane proteins provides a much smaller driving force for association than the tight packing of small residues (29–31). Thus, we expected the loose interface to be thermodynamically less stable and geometrically more flexible, which would facilitate the motion of ions through the bundle.

Molecular dynamics (MD) simulations were used to probe the stability and dynamics of the de novo designed structure. We embedded the model structure in a homogenous 1-palmitoyl-2-oleoylphosphatidylcholine bilayer with two Zn^{2+} fully occupying one of the 4Glu-2His sites; the other site was empty as described in the supplement. The fully bound site is electrically neutral when the coordinating residues are in their standard protonation states (charged Glu and neutral His). To explore the role of protonation at the unliganded site, we carried out four independent simulations exploring different possible charge states (fig. S2, A to C). Qualitatively, all four simulations behave similarly on the 100-ns time scale. The chelated di-zinc site is extremely stable and shows a Cα root mean square deviation (RMSD) of about 0.75 Å with very few fluctuations (fig. S2A, right). Water enters the transporter, providing hydration by 10 to 14 water molecules along the lumen between the two binding sites, a desirable feature for ion transport (fig. S2E). Analogous to a hydrophobic gate, bulky aromatic Phe14 adjacent to the Zn^{2+} site appears to partially exclude water.

Next, we examined the distance between the helices in the tight versus loose dimer interfaces. The helices in the tight dimer remain closely packed near the initial structure (red curves, Fig. 1E and fig. S2B). However, the distance between helices in the weak interface increases by as much as 3 Å in three of four simulations (fig. S2B). The separation in the weak dimer interface is most pronounced near the unoccupied metal-binding site. To test the influence of the metal ions on the stability of the structure, we initiated three simulations in which Zn^{2+} was removed from the binding site, with the carboxylates in three different protonation states (table S4). In each simulation, the tight dimer interface remained at a constant, close distance, whereas the loose dimer interfaces separated by up to 5 Å (fig. S2B). The findings suggest that metal binding is important for stabilizing the tetrameric bundle but not the tightly packed dimer. Although these simulations are much shorter than the time scale required for a transport cycle, they are consistent with the intended design of loose and tight interfaces, each interface with distinct roles in facilitating the positioning of side chains and providing a dynamic water like path for ion motion through the center of the transporter.

We used a battery of techniques to define the structural and dynamic characteristics of Rocker. The binding of metal ions and oligomerization was studied in micelles by using analytical ultracentrifugation (AUC) and solution nuclear magnetic resonance (NMR). The structure of the Zn^{2+}-free state was determined at high resolution by x-ray crystallography of Rocker solubilized in both micelles and monoolein lipidic cubic phase. Finally, the oligomeric state, topology, and Zn^{2+} binding were determined in phospholipid bilayers by solid-state NMR (SSNMR).

AUC showed that Rocker forms tetramers in a Zn^{2+}-dependent manner in dodecylphosphocholine (DPC) micelles. Equilibrium sedimentation curves were well described by an equilibrium between a tight dimer and a tetramer (fig. S3). Tetramerization is dominant only at a peptide-to-detergent ratio of 1:200 or higher in this medium, but the addition of excess Zn^{2+} shifted the equilibrium toward the tetrameric state at lower peptide/detergent ratios (supplementary material).

We crystallized Zn^{2+}-free Rocker from micelles, as well as the lipidic cubic phase, in a total of three nonisomorphous space groups and solved structures using data that extended between 2.7 and 2.8 Å (Fig. 2). Only the non-Zn^{2+} form of the protein has crystallized to date. The crystallographic structures solved by molecular replacement show a dimer formed by two tightly packed helices (Fig. 2, A and B). The conformations of the dimer in the three structures are nearly identical (Cα RMSDs between 0.60 and 0.84 Å), despite differences in crystal packing. The dimers are composed of straight α helices that interact along the tight interface with tight interdigitation of the small methyl groups of the alanine residues, as in the design. The His and Glu ligands are positioned with the potential to bind metals with a change in rotameric state (Fig. 2, B and C). The observed structure of the dimer is in good agreement with the designed tight dimer (Cα RMSD ranges from 2.3 to 2.6 Å). We attribute small deviations from the design to the lack of metal-ligand interactions in the experimental structure. Indeed, in the MD simulations of the Zn^{2+}-free structure, the dimers move 0.8 Å closer to the x-ray structure than the original design (fig. S2C).

The binding stoichiometry for Zn^{2+} was confirmed in solution by titrating Rocker with Zn^{2+} ions in DPC micelles under conditions where it is predominantly tetrameric (peptide/ detergent ratio = 1:100). Addition of Zn^{2+} resulted in a decrease in the intensities of aromatic resonances (including the chelating His residue) and an increase in a new set of peaks in the solution NMR spectra (Fig. 3A). The titration plateaus at two Zn^{2+} ions/ tetramer. Two sets of peaks in the spectrum indicate that the rate of dissociation and rebinding of Zn^{2+} to the side chains is slower than ~10ms. Beyond two equivalents, additional shifts are observed, but the change with respect to the Zn^{2+} concentration is more gradual and indicative of much weaker association of the metal ions with a second binding site. This behavior is consistent with the design, which anticipates negative cooperativity between the two sets of di-Zn^{2+}–binding sites.

Previous work with homo-tetrameric peptides shows that they are much more stable in phospholipid bilayers than DPC micelles (32, 33), so we turned to SSNMR to determine the structure and conformational dynamics of Rocker in phospholipid bilayers. One-dimensional (1D) ^{13}C cross-polarization (CP) magic angle–spinning (MAS) spectra of apo-Rocker in dimyristoylphosphatidylcholine (DMPC) bilayers from −40° to 40°C showed a single set of relatively narrow peaks (0.9 ppm Cα line widths) per carbon for four ^{13}C-labeled residues (Fig. 3B). The backbone ^{13}C chemical shifts reflect helical structure (fig. S4C). The line widths broaden with increasing temperature, which indicates that the peptide becomes mobile in the liquid-crystalline phase of the membrane. Dipolar coupling measurements yield ^{13}C-H order parameters of 0.84/0.84, 0.73/0.77, and 0.55/0.75 for Cα at Ala8/Ala22, L19, and I5 in apo/Zn^{2+}-bound states, respectively (fig. S4B), and all dephasing curves are asymmetric, which indicates global microsecond–time scale motion in both the apo and Zn^{2+} bound peptides (34, 35). The addition of Zn^{2+} ions had a strong influence on the SSNMR spectra of Rocker. In contrast to the apo sample, the Zn^{2+}-bound sample lacks the L19α-I5δ peak and has weaker A8/22-I5 and A8/22-L19 cross peaks, which indicate that Zn^{2+} binding loosens interhelical packing (Fig. 3C). Ion binding also caused noticeable chemical shift changes, which are particularly pronounced at A8 and A22 (Fig. 3C and fig. S4, D and E). Taken together, these results show a single conformation with substantial

dynamics on the microsecond time scale and significant Zn^{2+}-dependent structural perturbations.

To determine the oligomeric structure in DMPC bilayers, we conducted a ^{19}F spin diffusion experiment, Centerband-Only Detection of Exchange (CODEX), on Rocker singly labeled with *para*-^{19}F-phenylalanine (^{19}F-Phe) at position 14 [36, 37]. Distance-dependent interhelical ^{19}F-^{19}F dipolar coupling is manifested as a decay of a ^{19}F spin echo with increasing mixing time. The equilibrium value of the spin echo intensity is $1/n$, where n is the oligomer number of the assembly. The measured ^{19}F CODEX intensities (Fig. 3D and fig. S5) decayed to <0.4, which indicates that the assembly is larger than a dimer. The nonplanar quadrilaterals formed by ^{19}F-Phe modeled in the anticipated tetramer superposed with the crystallographic dimers resulted in excellent fits of the measured decay (Fig. 3D and fig. S5). A C_4 symmetrical array of ^{19}F nuclei gave an unsatisfactory fit, which ruled out a square planar model (fig. S5E). These results corroborate an antiparallel tetramer.

Conclusive support for an antiparallel tetramer was obtained from 2D ^{13}C correlation spectra. At a mixing time of 500 ms, cross peaks between L19 and I5 side chains were observed (Fig. 3C). These residues are found along the tight dimer interface, and, together with the ^{19}F-Phe interaction along the loose interface, confirm antiparallel association along both interfaces in bilayers.

Finally, to determine whether the designed peptide is embedded in the lipid bilayer, we measured 2D NMR spectra that correlate the lipid and water ^1H signals with the peptide ^{13}C chemical shifts [38, 39]. Lipid-peptide cross peaks were detected at short mixing times (< 36 ms) (fig. S4F), which indicates that the peptide is well inserted into the hydrophobic part of the membrane. The fast spin–diffusion buildup curves for both the lipid and water ^1H peaks (fig. S4G) indicate that the Rocker helical bundle spans the membrane and is well hydrated, likely by both the membrane-surface water and intra-channel water.

Two important characteristics of natural transporters are their substrate-selectivity and their ability to use one substrate's concentration gradient to drive the uphill transport of a second substrate. To test how Rocker meets these criteria, we conducted flux assays in large unilamellar vesicles (LUVs) in which we monitored Zn^{2+} and H^+ influx and efflux using fluorescent indicators (Fig. 4A and supplementary methods).

To test ion selectivity, we measured Rocker's ability to facilitate inward metal ion transport down a concentration gradient. As expected, Rocker conducts first-row transition metal ions Zn^{2+} and Co^{2+} but not the hard divalent ion, Ca^{2+}, which prefers higher-valent oxygen-rich ligand environments (Fig. 4B and fig. S6, A and B). Moreover, Ca^{2+} does not influence Zn^{2+} efflux (fig. S6A), and substitution of the Glu ligands to Gln greatly impairs Zn^{2+} efflux (Fig. 4B).

The rate of Zn^{2+} transport into vesicles follows Michaelis-Menten kinetics ($K_M = 280 \pm 90$ μM; $V_{max} = 1.1 \pm 0.1$ min^{-1}). For comparison, the K_M and rate of transport in the natural ZitB Zn^{2+} transporter are 105 μM and 142 min^{-1}, respectively [22, 40]. From the Irving-Williams [41] series (which approximately predicts the relative affinities of first-row transition metal ions for a given site) and the ligand environment of Rocker, we expected

that Co^{2+} should bind less tightly, which could lead to a higher K_M. Also, if ligand exchange is rate-limiting as suggested by the solution NMR spectra (Fig. 3A), the weaker binding affinity might be accompanied by an increase in V_{max}. Indeed, K_M for Co^{2+} increases to 1400 ± 200 μM and V_{max} increases to 470 ± 40 min^{-1} (Fig. 4, E and F, and fig. S6B).

We next tested Rocker's ability to cotransport Zn^{2+} and H^+. Rocker is able to use a Zn^{2+} gradient to drive the transport of protons uphill and into vesicles (Fig. 4C). Cotransport was measured by tracking both the downhill Zn^{2+} flux and the resulting H^+ flux as a function of the internal Zn^{2+} concentration. The rate of proton influx tracks with the rate of Zn^{2+} efflux, with a common K_M of 280 μM, which indicates that H^+ and Zn^{2+} transport are linked (Fig. 4, E and F). The proton-Zn^{2+} stoichiometry computed from the initial rates is three to four protons per Zn^{2+}. This finding is consistent with the guiding hypothesis that the binding of Zn^{2+} occurs with the concomitant displacement of protons. Moreover, Rocker functioned in a Zn^{2+}-proton antiport assay in the presence of a membrane permeable ion, NO_3^-, which eliminates the accumulation of electrical potentials (fig. S6C).

We also determined that a proton gradient is able to cause accumulation of Zn^{2+} up its own concentration gradient, when the initial concentrations of Zn^{2+} were identical on both sides of the vesicle. However, the efficiency of the process is far less than for the converse: Over 100 protons are transported for every Zn^{2+} transported. This finding suggests that there might be two competing mechanisms: The predominant one is diffusion of protons through Zn^{2+}-bound Rocker; the less-frequent path involves proton binding at the Zn^{2+} site and expulsion of a zinc ion. A possible explanation for the different behavior for Zn^{2+} compared with proton gradients is that the highly polar divalent Zn^{2+} is unable to diffuse through Rocker without binding to the coordination sites, which in turn would require deprotonation of the ligands. By contrast, protons could move along proton wires through the pore without requiring dissociation of the divalent metal ion. A possible reason for the proton-leakiness is the lack of a proton-impermeable hydrophobic gate, which appears to be important for tight coupling in much larger and highly evolved proton-dependent transporters. Future designs will aim to achieve a transporter function similar to that of native proteins. Nevertheless, these findings, along with the very simple structure of Rocker, provide support for the view that transporters may have evolved from very simple pseudo-symmetric precursors (42).

The structural and functional characterization of Rocker indicates that the design community has now passed an important milestone; the first high-resolution structure of a designed membrane protein has been determined through a combination of x-ray crystallography and NMR. Our design strategy combined the strengths of traditional computational design techniques with biophysically motivated conformational ensemble–based reasoning. Although Rocker's activity falls short of natural transporters, it remains significant that function was achieved without high-throughput screening or directed evolution—and bodes well for future investigations in which computational design is combined with these powerful experimental methods.

Supplementary Material

Refer to Web version on PubMed Central for supplementary material.

ACKNOWLEDGMENTS

REFERENCES AND NOTES

1. Koga N, et al. Nature. 2012; 491:222–227. [PubMed: 23135467]

2. Zastrow ML, Pecoraro VL. Coord. Chem. Rev. 2013; 257:2565–2588. [PubMed: 23997273]

3. Tinberg CE, et al. Nature. 2013; 501:212–216. [PubMed: 24005320]

4. Reig AJ, et al. Nat. Chem. 2012; 4:900–906. [PubMed: 23089864]

5. Zastrow ML, Peacock AFA, Stuckey JA, Pecoraro VL. Nat. Chem. 2012; 4:118–123. [PubMed: 22270627]

6. Zastrow ML, Pecoraro VL. J. Am. Chem. Soc. 2013; 135:5895–5903. [PubMed: 23516959]

7. Kiss G, Çelebi-Ölçüm N, Moretti R, Baker D, Houk KN. Angew. Chem. Int. Ed. Engl. 2013; 52:5700–5725. [PubMed: 23526810]

8. Korendovych IV, et al. J. Am. Chem. Soc. 2010; 132:15516–15518. [PubMed: 20945900]

9. Perez-Aguilar JM, Saven JG. Structure. 2012; 20:5–14. [PubMed: 22244752]

10. Radestock S, Forrest LR. J. Mol. Biol. 2011; 407:698–715. [PubMed: 21315728]

11. Jardetzky O. Nature. 1966; 211:969–970. [PubMed: 5968307]

12. Mitchell P. Nature. 1957; 180:134–136. [PubMed: 13451664]

13. Morrison EA, et al. Nature. 2012; 481:45–50. [PubMed: 22178925]

14. DeGrado WF, Wasserman ZR, Lear JD. Science. 1989; 243:622–628. [PubMed: 2464850]

15. Lear JD, Wasserman ZR, DeGrado WF. Science. 1988; 240:1177–1181. [PubMed: 2453923]

16. Hong M, DeGrado WF. Protein Sci. 2012; 21:1620–1633. [PubMed: 23001990]

17. Pasternak A, Kaplan J, Lear JD, Degrado WF. Protein Sci. 2001; 10:958–969. [PubMed: 11316876]

18. Crick FHC. Acta Crystallogr. 1953; 6:685–689.

19. Grigoryan G, Degrado WF. J. Mol. Biol. 2011; 405:1079–1100. [PubMed: 20932976]

20. Summa CM, Lombardi A, Lewis M, DeGrado WF. Curr. Opin. Struct. Biol. 1999; 9:500–508. [PubMed: 10449377]

21. Lombardi A, et al. Proc. Natl. Acad. Sci. U.S.A. 2000; 97:6298–6305. [PubMed: 10841536]

22. Chao Y, Fu D. J. Biol. Chem. 2004; 279:17173–17180. [PubMed: 14960568]

23. Grigoryan G, Reinke AW, Keating AE. Nature. 2009; 458:859–864. [PubMed: 19370028]

24. Grigoryan G. J. Comput. Chem. 2013; 34:2726–2741. [PubMed: 24132787]

25. Lazaridis T. Proteins. 2003; 52:176–192. [PubMed: 12833542]

26. Senes A, et al. J. Mol. Biol. 2007; 366:436–448. [PubMed: 17174324]

27. Schramm CA, et al. Structure. 2012; 20:924–935. [PubMed: 22579257]

28. Summa CM, Rosenblatt MM, Hong JK, Lear JD, DeGrado WF. J. Biol. Biol. 2002; 321:923–938.

29. Zhang Y, Kulp DW, Lear JD, DeGrado WF. J. Am. Chem. Soc. 2009; 131:11341–11343. [PubMed: 19722646]

30. Unterreitmeier S, et al. J. Mol. Biol. 2007; 374:705–718. [PubMed: 17949750]

31. Moore DT, Berger BW, DeGrado WF. Structure. 2008; 16:991–1001. [PubMed: 18611372]

32. Cristian L, Lear JD, DeGrado WF. Proc. Natl. Acad. Sci. U.S.A. 2003; 100:14772–14777. [PubMed: 14657351]

33. MacKenzie KR, Fleming KG. Curr. Opin. Struct. Biol. 2008; 18:412–419. [PubMed: 18539023]

34. deAzevedo ER, et al. J. Chem. Phys. 2008; 128:104505. [PubMed: 18345904]

35. Cobo MF, Achilles A, Reichert D, Deazevedo ER, Saalwächter K. J. Magn. Reson. 2012; 221:85–96. [PubMed: 22750254]

36. deAzevedo ER, Hu W-G, Bonagamba TJ, Schmidt-Rohr K. J. Am. Chem. Soc. 1999; 121:8411–8412.

37. Buffy JJ, Waring AJ, Hong M. J. Am. Chem. Soc. 2005; 127:4477–4483. [PubMed: 15783230]

38. Huster D, Yao X, Hong M. J. Am. Chem. Soc. 2002; 124:874–883. [PubMed: 11817963]

39. Hong M. Structure. 2006; 14:1731–1740. [PubMed: 17161364]

40. Chao Y, Fu D. J. Biol. Chem. 2004; 279:12043–12050. [PubMed: 14715669]

41. Irving RJPWH, Williams RJP. J. Chem. Soc. 1953:3192–3210.

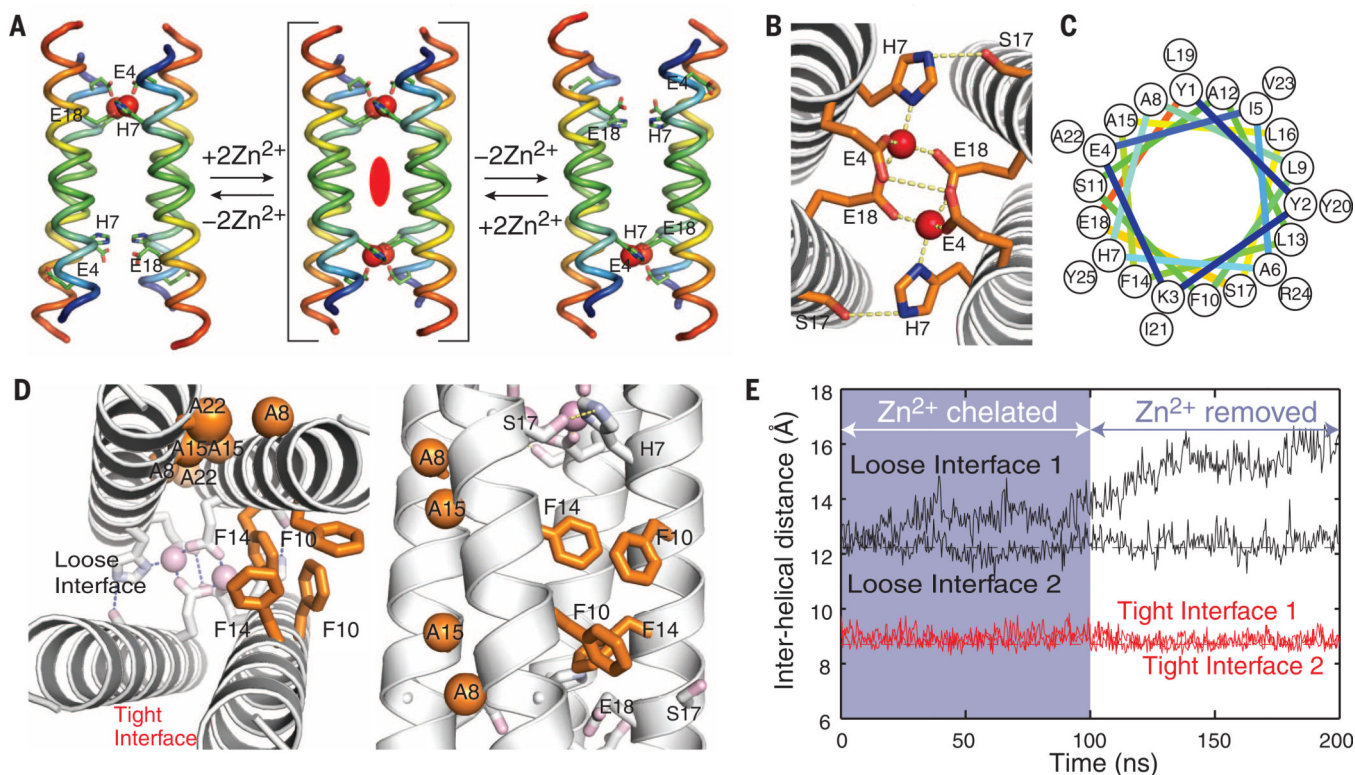42. Rapp M, Granseth E, Seppälä S, von Heijne G. Nat. Struct. Mol. Biol. 2006; 13:112–116. [PubMed: 16429150]

Fig. 1. Computational design and molecular dynamics simulations of Rocker

(**A**) Schematic of the goal of obtaining conformational exchange between two oppositely oriented symmetry-frustrated states without being trapped in a symmetric state with both sites simultaneously occupied. (**B**) Metal site consists of a set of ExxH motifs and a single Glu residue from each of the tight dimers. (**C**) Helical-wheel diagram of Rocker peptide. (**D**) The repacking algorithm placed Ala residues at the tight interface and Phe residues at the loose interface. Empty metal site on the left is omitted for clarity. (**E**) MD simulation of the design model with two Zn^{2+} ions placed at one metal site show stable interhelical distances for both tight and loose interfaces. Continuing the simulation after removing the Zn^{2+} ions maintained the tight interfaces, but resulted in an increased interhelical distance at the loose interface.
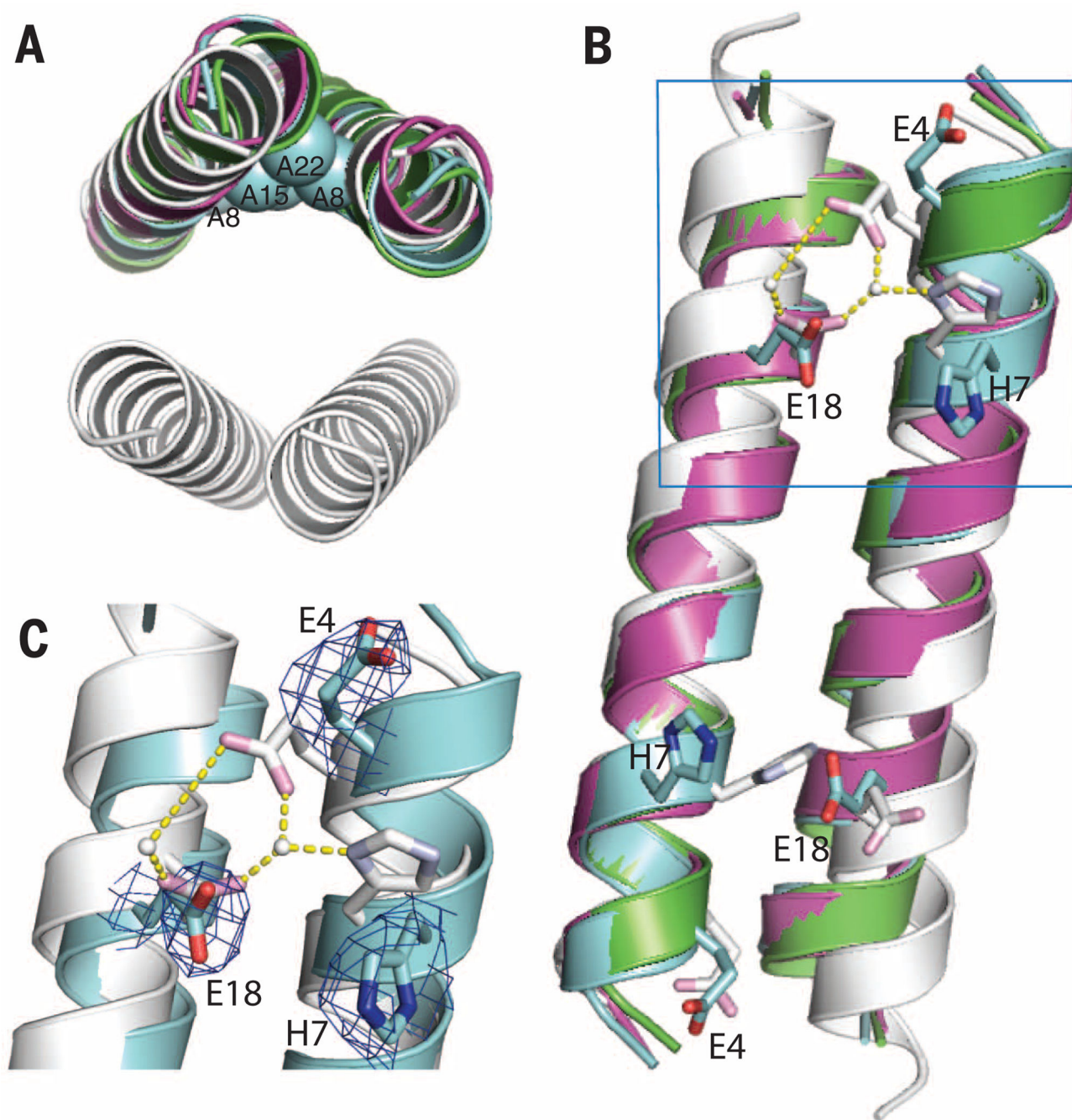
Fig. 2. Structure of Rocker

(**A**) Axial view of the x-ray crystal structures from three different packing environments (green, cyan, and magenta for space groups of increasing symmetries, $P4_32_12$, $I4_122$, and $I2_13$, respectively) superimposed on the tight dimeric subunit of the design model (white), with the Ala residues (spheres from the cyan structure with highest resolution of 2.7 Å) forming the tight interface as anticipated. (**B**) Metal-binding residues (sticks) from the crystal structures can chelate with a change in rotamers without encountering any

unfavorable steric interactions within the dimer. (**C**) A close-up of the metal site with $2mF_{obs} - DF_{calc}$ map contoured at 1.0 σ for the 2.7 Å–resolution structure.
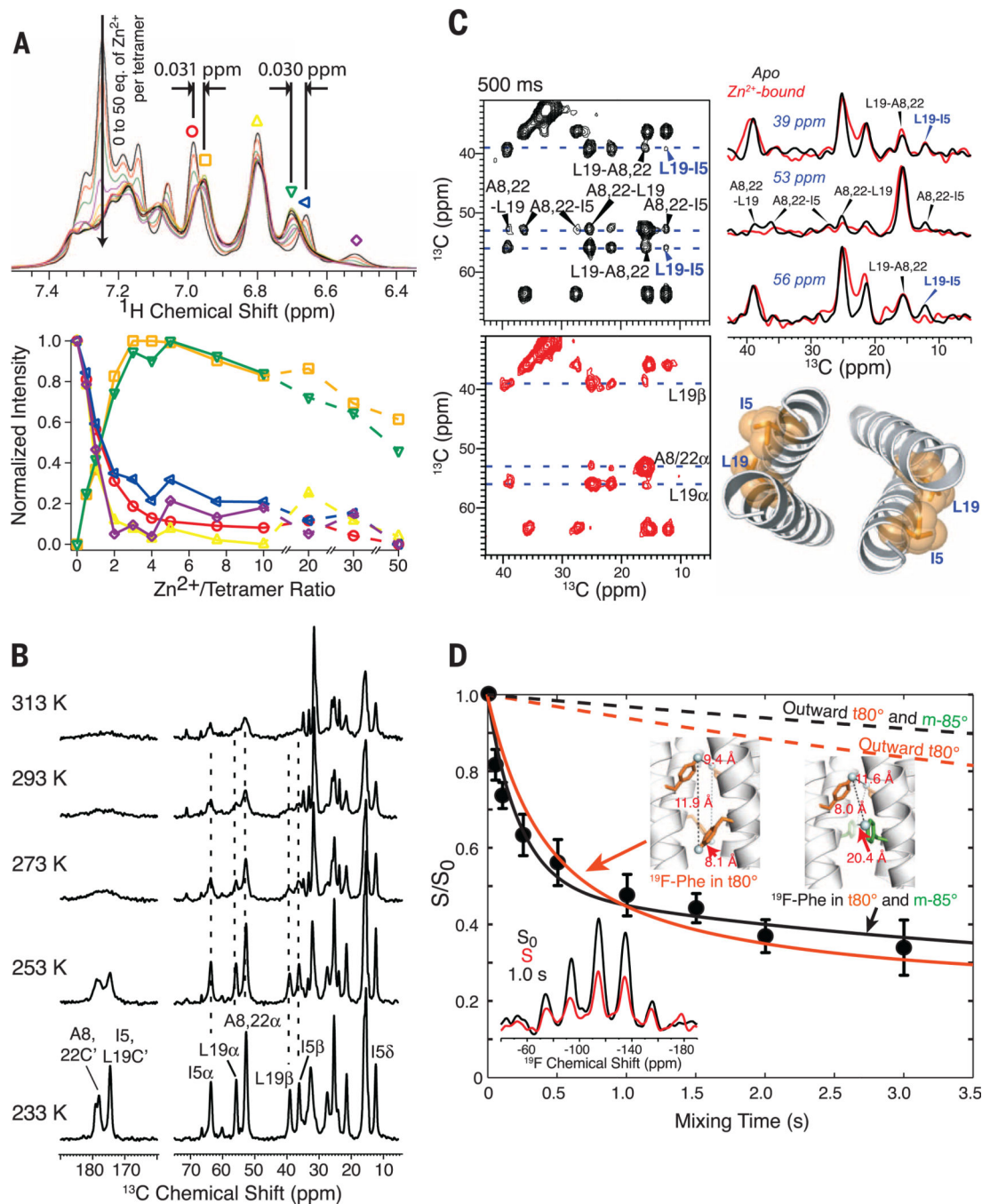
Fig. 3. Evidence for Zn²⁺ binding and tetramerization of Rocker in micelles and lipid bilayers
(**A**) ¹H-NMR of Rocker in D_2O and deuterated DPC (at 900 MHz ¹H field) shows significant changes to the side-chain chemical shifts as Zn^{2+} is titrated into the solution. The changes level off when Zn^{2+} reaches two equivalents per tetramer, which indicates the expected binding stoichiometry. (**B**) 1D ¹³C CP-MAS spectra of apo Rocker in DMPC bilayers from 233 K to 313 K show invariant peak positions across a wide temperature range, which indicates single species with conformational dynamics in bilayers. (**C**) 2D ¹³C-¹³C 2D correlation spectra of apo and Zn^{2+} bound Rocker with 500-ms mixing.

Relevant 1D cross sections are plotted to compare cross-peak intensities. L19-I5 cross peaks (blue annotations) are observed, indicating antiparallel packing. Compared with the apo sample, the Zn^{2+}-bound sample lacks the L19α-I5δ peak in the 56-ppm cross section and has much weaker A8/22-I5 and A8/22-L19 cross peaks, which indicate that Zn^{2+} binding loosens interhelical packing. The proximal L19 and I5 are shown on a structural model of Rocker. (**D**) ^{19}F CODEX data of DMPC-bound Rocker with *para*-^{19}F-Phe14 at 220 K and 8 kHz MAS (error bar, SD propagated from signal-to-noise). The CODEX intensity decays to $1/n$ of 0.34, where n is the oligomer number; this indicates that the peptide assembles into a species larger than dimers. The CODEX decay is well fit (solid lines) using ^{19}F-^{19}F distances found in inward-facing rotamers of Phe14 in an antiparallel tetramer, consistent with the crystal structures. The data rule out outward-facing orientations of Phe14 (dashed lines), which suggests that Glu4 and Glu18 face the pore.
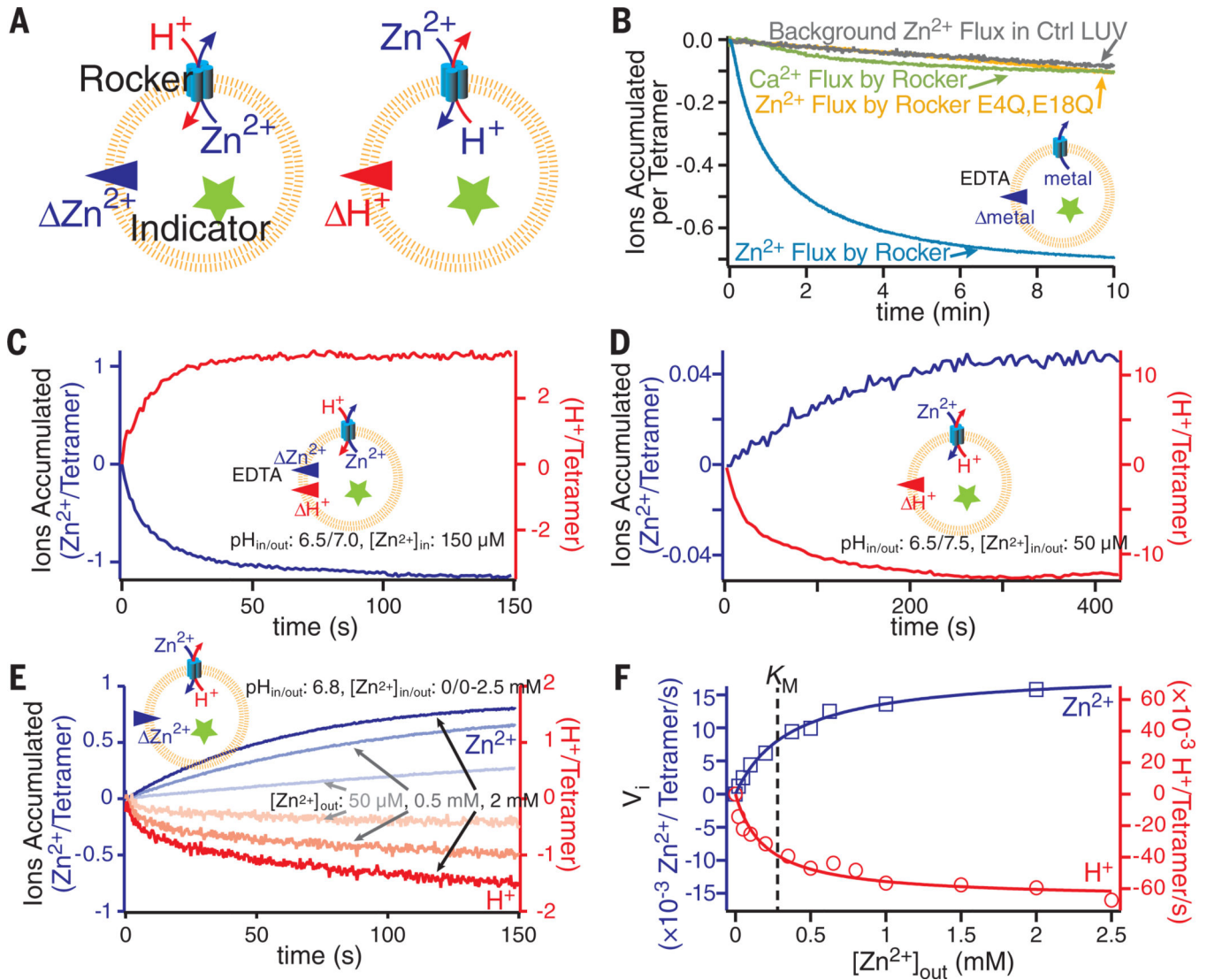
Fig. 4. Antiporter-like function of Rocker

(**A**) Examples of liposome flux assays using fluorescent indicators for characterizing the cotransportation function are illustrated. (**B**) Ion selectivity in Rocker is shown via a Zn^{2+} efflux assay. Rocker can specifically transport Zn^{2+} (blue) but not Ca^{2+} (green), at a level higher than passive leakage (gray). Mutating the first-shell ligands via E4/E18-to-Q substitutions abrogates Zn^{2+} transport (gold). (**C**) Rocker-mediated, outward $[Zn^{2+}]$ gradient-driven proton-antiport against an outward pH gradient is shown by measuring net inward proton flux (red, right axis) and the outward Zn^{2+} flux (blue, left axis). (**D**) Rocker-mediated, H^+-driven Zn^{2+} antiport under symmetrical Zn^{2+} concentration is shown using both the outward proton flux (red, right axis) and the inward Zn^{2+} flux (blue, left). (**E**) Representative traces show the dependence of initial rates of transport on the exterior Zn^{2+} concentration. (**F**) The initial rates of transport of Zn^{2+} and H^+ from panel (E) increase with increasing exterior Zn^{2+} concentration, following Michaelis-Menten kinetics with a K_M of ~ 280 μM. (Error values in text are SD propagated from curve fitting.)